

Tri-coupler geometries for achromatic nulling interferometry in the near infrared

HARRY-DEAN KENCHINGTON GOLDSMITH,^{1,*} NEMANJA JOVANOVIĆ,²
ANUSHA PAI ASNODKAR,² YOO JUNG KIM,³ AHMED SANNY,³ PRADIP
GATKINE³ AND MICHAEL P. FITZGERALD³

¹*Astrophotonics Australia, Canberra, ACT, Australia*

²*Department of Astronomy, California Institute of Technology, 1200 East California Boulevard, Pasadena, 91125, CA, USA*

³*Physics & Astronomy Department, University of California, Los Angeles, 475 Portola Plaza, Los Angeles, 90095, CA, USA*

*harrykenchington@astrophotonics.com.au

Abstract: Astrophotonics will be central to the next generation of astronomical instrumentation, enabling lightweight, compact, and environmentally stable systems for both ground-based observatories and future space missions. One key application is beam combination for nulling integrated with a photonic lantern, and long baseline nulling interferometry, which suppresses starlight to reveal exoplanets and companions. Compact, broadband photonic beam combiners are essential for providing a pathway to complex circuitry incorporated into a single chip and scalable solutions for single and multi-telescope instruments, and are investigated herein.

Two-waveguide photonic combiners rely on symmetric evanescent coupling to interfere light, which is inherently chromatic and requires modification for broadband operation. A three-waveguide configuration, or tri-coupler, offers the potential for deeper, broader, and more stable achromatic nulls compared with two-waveguide approaches. This work compares the simulated performance of two evanescent tri-couplers and a multimode interference coupler (MMI) across the 1.5–1.8 μm band, evaluating exoplanet throughput, starlight attenuation, sensing characteristics, and estimations on fabrication tolerance. The standard tri-coupler was outperformed by both a bespoke tapered tri-coupler and the MMI, each of which had an exoplanet throughput $>85\%$ over the band compared to the standard design, recording a minimum exoplanet throughput of 50% at the waveband extremes. The tapered tri-coupler was further redesigned to achieve a non-degenerate sensing state. The MMI, while limited to a starlight attenuation of 40 dB (10^{-4}) by uncoupled light, showed the greatest tolerance to fabrication errors, offering strong practical potential.

Future designs aim to combine high exoplanet throughput, deep starlight attenuation, and non-degenerate sensing within a single integrated architecture. A complex integrated circuit is the goal of many astrophotonic projects, and these components will be used for beam combination, potentially after a photonic lantern or before an on-chip spectrometer, or both.

1. Introduction

The first exoplanet was detected in 1992 [1] using an indirect detection method — pulsar timing. Since then, >6000 exoplanets have been confirmed (as of November 2025 from NASA’s exoplanet archive) predominantly via indirect techniques such as transit and radial velocity methods. Direct detection approaches, including coronagraphy and interferometry, account for only a fraction of detections and typically identify large, young exoplanets and brown dwarfs that remain luminous due to their thermal emission. The closer an exoplanet orbits its host star, the more difficult it becomes to disentangle planetary light from the overwhelming stellar glare. As a result, direct imaging is currently most effective for exoplanets at wide separations — tens to thousands of astronomical units. To probe closer orbits and detect fainter companions, new starlight suppression techniques are required.

Starlight suppression has two main pathways: coronagraphy and nulling interferometry. Coronagraphy uses bulk optical components to block on-axis starlight [2] while allowing off-axis planetary light through. Achieving small inner working angles requires sophisticated coronagraph designs, which are technically demanding. In contrast, nulling interferometry employs destructive interference between two beams from segmented or multiple telescopes.

Beam combination in the pupil plane creates bright and dark fringes corresponding to phase differences across the sky. A 180° phase shift between telescopes suppresses on-axis starlight while maintaining off-axis sources, such as exoplanets, in bright fringes [3].

Nulling applications include exoplanet detection and characterization. The required starlight suppression depends on the exoplanet investigated. For example, the planet-star flux ratios range for a close-orbit hot Jupiter or young, self-luminous, gas giants still in the process of forming is $\sim 10^{-4}$ [4], whereas a cool Earth-like potentially habitable exoplanet is 10^{-10} at the $1.55 \mu\text{m}$ wavelength. High contrast instrumentation is also needed for direct detection of close-orbit low mass stars and brown dwarfs (10^{-2}) [5]. Nulling in a Photonic integrated circuit (PIC) exploits the wave nature of light to achieve precise interference; photonic beam combiners are natural candidates for nulling interferometry [6] and after a photonic lantern [7].

Astrophotonics [8–11] is an emerging field that leverages photonic technologies developed by universities, research centers, and the telecommunications industry to manipulate light in waveguides and fibers before a science camera. These devices enable on-chip starlight suppression for direct exoplanet detection. PICs are already deployed at observatories: GRAVITY serves as the beam combiner for the Very Large Telescope Interferometer (VLTI) [12], and the Fibered Imager for a Single Telescope (FIRST)-PIC [13, 14] is installed at the Subaru Telescope. The latter uses $H\alpha$ emission detection [15, 16] for brown dwarf identification. The Guided Light Interferometric Nulling Technologies (GLINT) [17], installed at the Subaru Telescope, is a photonic nulling interferometry instrument [18]. The Nulling Observations of exoplanets and dust (NOTT) instrument is another nulling interferometer that employs a PIC to increase the null depth and operates in the mid-infrared at the VLTI [19, 20]. These photonic examples show the breadth of current astrophotonics. When fabricating these photonic chips, the choice of beam combiner is a critical step in PIC design, with coupler selection restricted by materials and fabrication methods.

The NOTT instrument employs directional couplers [21]. With careful design, evanescent directional couplers can be made nearly achromatic, as demonstrated in the predecessor to the GLINT instrument [22]. A configuration of three identical, evanescently coupled waveguides – a tri-coupler – may offer superior achromatic nulling. For a 3D structure, injecting equal-intensity asymmetric (at a 180° phase difference) light into two waveguides will produce a null in the third waveguide. For a planar device, the two outer nulling requires light injected into the outer waveguides. Chromaticity in the input phase difference will affect this null. Achromatic phase shifters [23] are being developed, but this was not the focus of this paper. Previous tri-coupler demonstrations have utilized ultrafast laser inscription (ULI) in bulk glass, a low-index-contrast technology ($\Delta n \approx 0.001$) that enables low-loss, three-dimensional waveguides [24]. However, this technology requires large bend radii that will limit scalability.

In contrast, high-index-contrast material systems ($\Delta n > 0.1$) fabricated via thin-film lithography enable compact two-dimensional waveguides with tight bend radii, enhancing scalability. However, these often suffer from higher coupling losses due to mode mismatch with standard optical fibers. Upcoming facilities such as the Giant Magellan Telescope (GMT) [25] and the Habitable Worlds Observatory (HWO) [26] will require compact, densely integrated photonic circuits, making high-index-contrast technologies increasingly attractive. Multimode Interference couplers (MMIs) have been demonstrated in these materials for broadband beam splitting in astrophotonic applications [27–29]. Their tolerance to fabrication errors [30] makes them competitive with evanescent couplers, though typically at the cost of lower throughput. Thus,

the optimal choice of coupler strongly depends on the refractive index contrast of the chosen platform.

The present work uses lithographically fabricated waveguides – a silica substrate with a deposited germanium-doped silica core layer and a silica top layer. At this index difference ($\Delta n \approx 0.03$), the waveguides have efficient fiber coupling of approximately 5%, minimized dispersion, low loss, and polarization independence when employing square waveguides [31]. At this refractive index contrast, both evanescent and MMI-based couplers are viable candidates.

Following previous work on nulling interferometry [18] for three-dimensional tri-couplers, two-dimensional tri-couplers are evaluated in this work as nulling interferometers. While typically consisting of three evanescently coupled waveguides, the term tri-coupler in this work is extended to include any three-input, three-output device, such as a 3×3 MMI. Three designs are compared in this work (Sec. 2): a standard tri-coupler with three equal-width waveguides coupled evanescently, a custom-made 3×3 MMI, and a bespoke tapered tri-coupler inspired by Hsiao et al. [32].

The comparative performance of these devices is evaluated in terms of exoplanet throughput (Sec. 3.1), starlight suppression (Sec. 3.4, component losses (Sec. 3.2) including bend loss, and sensing (Sec. 3.3). Null depth limitations, fabrication tolerances, and the resulting starlight suppression are discussed in Sec. 3.4. These metrics provide a realistic assessment of these tri-couplers as nulling beam combiners and their expected on-chip performance.

2. Tri-couplers

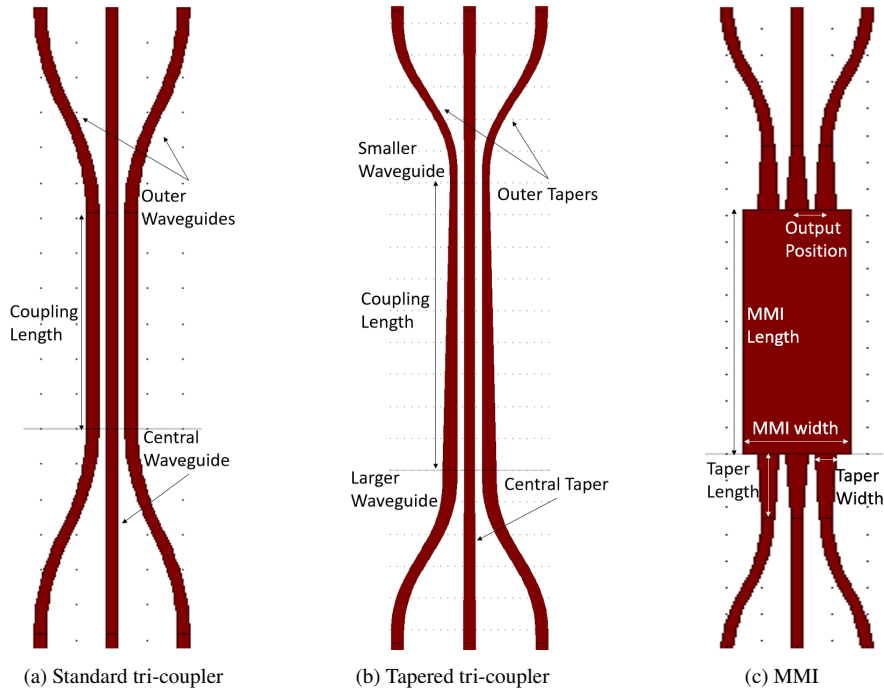


Fig. 1. The RSoft CAD of the three tri-couplers (not to scale).

Three tri-coupler configurations were investigated for use in on-chip nulling interferometry: a standard evanescent tri-coupler, a tapered tri-coupler, and a multimode interference coupler (MMI). Each design demonstrates the capability to form an on-chip null while balancing compactness, achromaticity, and fabrication feasibility. The three Computer-Aided Designs (CADs) used for

this work are shown in Fig. 1.

RSoft CAD and BeamPROP (version 2021.09) are interactive photonic design and beam propagation simulation programs, respectively [33], and were used to simulate the components included in this work. The default waveguide size, used at the input and output of each device, was $3.4 \times 3.4 \mu\text{m}$. These waveguides were simulated as completely square. Lithographically fabricated waveguide sidewalls have an expected 1° sidewall deviation, with minor impact on performance and birefringence. However, we ignore this for simplicity, which is sufficient to understand the basic characteristics of these devices. Birefringence is thus negligible [31].

Each simulation was undertaken using transverse electric (TE) mode fields in a 3-D semi-vector configuration. Full-vector was not used because polarization transfer was not expected. The built-in simulation material (SiO₂: n-index = 1.444 at $1.55 \mu\text{m}$) was lossless, with a 2% index contrast to the core material. At these wavelengths, the default waveguide is single-mode with an effective index of 1.458 at $1.55 \mu\text{m}$, but, as will be shown, the simulated components may include multimode components. This model and these parameters were used to be consistent with previous work [31]. The bend radius was set to $850 \mu\text{m}$ to minimize the tri-couplers' footprint, with a 3.5% loss (0.16 dB) per bend junction, and, as will be shown discussed in Sec. 3.2 is too small for this work but acceptable for characterizing these tri-coupler's for nulling.

All three tri-couplers have three input waveguides and three output waveguides (one central and two outer). In practice, only the outer input waveguides are routed to the edge of the chip for star/planet light injection (the center only used for testing purposes), and all three output waveguides are routed to the chip's end for detection. The existence of all three waveguides is critical in the interaction regions of the standard and tapered tri-coupler variants due to evanescent coupling occurring in the bends.

2.1. Nulling interferometry using tri-couplers

The tri-coupler suppresses starlight at the device's central output. This occurs only in a tri-coupler when equal-intensity electric fields with a 180° phase difference are injected into two of the three input waveguides. This choice is agnostic for three-dimensional symmetrical tri-couplers, but for two-dimensional tri-couplers, light must be injected into the outer waveguides. The latter is therefore the configuration for the unwanted starlight in this work. All light will undergo this injected phase difference to propagate through the tri-coupler, but objects spatially separated from the star have a phase offset.

The exoplanet is off-axis in the focal plane; its beam has a tilted wavefront in the pupil plane, resulting in the phase offset to the star. A known exoplanet can be positioned at the peak of a light fringe, at $\lambda/2D$, where λ is the observing wavelength and D denotes either the telescope diameter or the largest interferometric baseline. If the beams were injected into the tri-coupler in the pupil plane, it would mean that an exoplanet at $\lambda/2D$ would have an extra 180° (i.e., $\lambda/2$) phase difference compared to the on-axis starlight (without a phase tilt). How exoplanet light behaves in the PIC depends on the injection system, and optimizing for exoplanet light for all systems is beyond the scope of this work. For simplicity, we assume, for a two-telescope system, an achromatic 180° phase difference is implemented to attenuate starlight, and an exoplanet is positioned for a 0° phase difference. An equal intensity of light is assumed.

The simulations conducted in this work identified the design parameters for a starlight attenuation, defined as:

$$\text{Attenuation (dB)} = \eta_S = -10 \log_{10} \left(\frac{\text{Destructive output}}{\sum \text{All outputs}} \right) \quad (1)$$

which excludes exoplanet light throughput (η_P) and is distinct from the null depth (the ratio between destructive and constructive outputs). To understand how these metrics determine exoplanet detection, we consider the signal-to-noise (S/N) ratio of a starlight suppression device.

$$\text{Signal-to-noise} \propto \frac{S_p}{\sqrt{S_s}} \propto \frac{\eta_p}{\sqrt{\eta_s}} \quad (2)$$

that directly compares a detector's signal (S) from the exoplanet (p) and star (s) and the PIC throughput (η) [34]. This equation is sufficient to demonstrate that S/N is related to the PIC throughput. Hence, the tri-coupler design not only requires a deep attenuation but also a high exoplanet throughput. The null depth typically used in nulling interferometry [35], and other high contrast imaging, is defined as

$$\text{Null depth (dB)} = -10 \log_{10} \left(\frac{\text{Destructive output}}{\text{Constructive output}} \right) \quad (3)$$

The simulations in this work are normalized to the total injected light. Exoplanet and starlight simulation results are further normalized to the total output light (ignoring loss). The constructive interference is thus ≈ 1 units (the lowest being 0.5 units in this work), making little difference between Eq. (1) and (3). Hence, the attenuation will be used throughout this paper.

After the PIC, the star-to-planet contrast can be increased through self-calibration techniques [36] or using high-dispersion spectroscopy [37] up to the photon noise limit. The implication is that having a complete attenuation of the star in the PIC is not necessary when post-processing is available. Thus, the focus of this paper is a comparison between three tri-couplers' starlight attenuation (destructive output), exoplanet transmission (constructive output), and overall loss.

2.2. Tri-coupler Designs for Nulling

Starlight attenuation is maximized when equal-intensity fields are injected into the tri-coupler's output waveguides with a 180° phase offset. This maximum attenuation at 180° offset should be achromatic. Exoplanet throughput into the central output port is maximized when equal intensity fields are injected into the outer tri-coupler waveguides at a 0° phase offset. This is naturally chromatic. Hence, the length of each coupler was set to maximize the exoplanet light into the central port, where starlight is attenuated. The exception to this was the tapered tri-coupler that required a systematic approach to probing the parameter space to maximize the exoplanet light.

A simple method for identifying the exoplanet's light throughput is to run the couplers in reverse, treating them as 50:50 splitters: reversing the simulation to inject a beam into the central port and determining the length at an equal split. Splitting the light maximally into the outer ports, primarily by alternating the coupler's length, corresponds to the coupler length that maximizes the exoplanet light when injecting into the outer input ports and subsequently coupling into the central output port. Future experimental verification will use this as a quick method to test exoplanet throughput and achromaticity. Examples of the splitting ratio, the maximized exoplanet light into the central output port, and the starlight extinction in the central output for each tri-coupler are shown in Fig. 2. The bends employed before the input and output ports – Cosine S-bends for lower losses at a small length [38] – have a minimum $850 \mu\text{m}$ radius to maximize compactness with the tradeoff of radiative losses. All other parameters were optimized for throughput with compactness as a secondary priority.

Determining the standard tri-coupler length is equivalent to calculating the beat length (L_π), which is the length at which the initial field distribution completely transfers to the other waveguides — Light in the central waveguide splitting into the two outer waveguides for example. When injecting light into the central waveguide, L_π is described as [39]:

$$L_\pi = \frac{\lambda}{n_A - n_B} \quad (4)$$

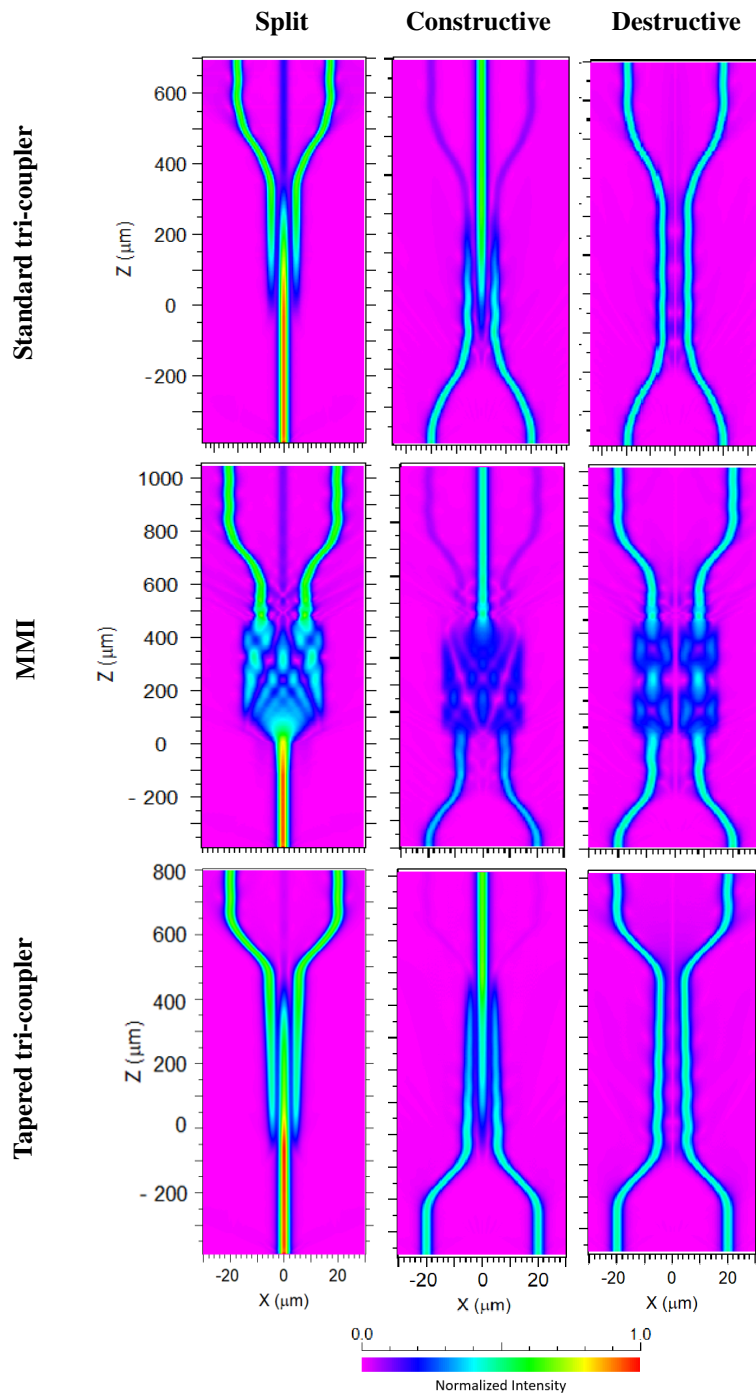


Fig. 2. Normalized intensity in the three tri-coupler configurations (Standard, MMI, and Tapered) for the splitting of a single input (Split), the constructive interference in the coupler for two equal intensity inputs with a 0° phase offset (Constructive), and the destructive interference for two equal intensity inputs with a 180° phase offset (Destructive).

where n_A and n_B are the effective indices for the standard tri-coupler's two symmetric modes (ignoring the one antisymmetric mode), and λ is the wavelength. The modes for a standard tri-coupler with a $2\ \mu\text{m}$ edge-to-edge gap between the waveguides, to maximize mode coupling and reduce the total device length while maintaining a beat length that is several orders of magnitude longer than the wavelength, were calculated for an approximate length. Iterative simulations determined that the coupling length for maximum exoplanet throughput into the central output waveguide, at $1.55\ \mu\text{m}$, was $308\ \mu\text{m}$.

Simulations at $1.55\ \mu\text{m}$ (Fig. 2) confirm the expected reciprocal behavior. When symmetric equal fields are launched into the outer ports, it directs light into the central output port, maximizing off-axis light coupling. In contrast, asymmetric equal fields (those with a 180° phase offset) will produce destructive interference of the starlight. This configuration demonstrates a stable destructive interference throughout the length, indicating achromatic behavior (see the third column of Fig. 2). However, the maximized exoplanet throughput will exhibit wavelength dependence based on Eq. (4).

To mitigate this chromaticity in exoplanet throughput, the outer waveguides were linearly tapered (in the third row of Fig. 2) along the coupling region, following the approach of Hsiao et al. [40]. For a finite-length tapered tri-coupler, a careful design of coupling constant and propagation constant (that change in z -position) will result in the coupler's supermodes' self-interference such that the central waveguide's local mode is solely illuminated at the output. There is no analytical solution for the tapered tri-coupler, though progress has been made for tapered directional couplers [41–43]. Hence, the tri-coupler parameters were determined through a systematic optimization procedure.

- Begin with a design with a large W_L/W_S contrast and extended interaction length
- Identify the position at which light concentrates in the central waveguide
- Set the new design at this interaction length, and the corresponding W_L
- Undertake a broadband simulation of exoplanet throughput to determine achromaticity
- Increase W_S and repeat until a wide bandwidth is not improved

This was undertaken for central waveguide widths of 2.8 , 3 , and $3.2\ \mu\text{m}$ (a parameter space restricted by simulation time).

The tapered tri-coupler (Fig. 1b) used a $450\ \mu\text{m}$ coupling length with the central waveguide fixed at $2.8\ \mu\text{m}$, while the outer arms decreased linearly from $4.0\ \mu\text{m}$ to $2.0\ \mu\text{m}$. This geometry maintains single-mode operation while achieving partial L_π achromatization (see Sec. 3).

The corresponding simulation (Fig. 2) demonstrates the same reciprocal nulling response as the standard tri-coupler. However, because the taper introduces asymmetry between the outer arms, the optimal configuration depends jointly on the taper gradient, coupling length, and central waveguide width. Although longer tapered structures can enhance achromaticity [41, 44], the device presented here was designed for compactness, balancing broadband performance with chip-scale integration requirements. Tapered bends were employed at the input and output to connect to $3.4\ \mu\text{m}$ access waveguides, introducing minor additional loss (see Sec. 3.2) relative to the standard tri-coupler.

An alternative broadband approach employs a multimode interference coupler (MMI). The behavior of which is calculated using constructive and destructive interference of the multiple (> 20) excited modes [45]. The positions of self-images along the MMI length (L) are given by

$$L = \frac{M}{N} \frac{4nW^2}{\lambda}, \quad (5)$$

where n is the core refractive index, W is the MMI width, N is the number of images (for example, $N = 2$ to split an input into two images), and M is the iteration of that number of images ($M = 1$ for the first iteration and thus the shortest length), where M and N are relatively prime integers.

Figure 2 shows that when the MMI’s two output ports are injected with equal-intensity electric fields having a 180° phase offset, it exhibits a central null analogous to that of the evanescent tri-couplers. Unlike those devices, however, the MMI’s null depth varies with length as the internal modes alternate between forming two and four images, seen in the second row, third column of Fig. 2. From Eq. (5), this length dependence implies a wavelength dependence, discussed further in Sec. 3.4.

A $30\text{ }\mu\text{m}$ -wide MMI was determined through simulation to be the smallest viable width (without eliciting evanescent coupling between input/output waveguides), and a device length of $440\text{ }\mu\text{m}$ produced near-equal splitting between outer ports when the central port was illuminated, corresponding to maximum constructive interference into the central port for two input electric fields into the outer ports with a 0° phase offset. This length corresponds to a symmetrical MMI mode [46] that reduces the length to a quarter of what is calculated in Eq. (5) (for $M = 1$ and $N = 2$).

Launching into the outer waveguides won’t benefit from the reduced MMI length and as such corresponds to a general interference MMI (L calculated using eq.5) for an $N = 8$ — producing eight images. Adjusting the outer port positions enabled coupling into special MMI configurations that yield three images when light enters either outer waveguide.

Table 1. MMI image formation at specific lengths, from Eq. (5), for different input positions (where $x = 0$ is the MMI’s center).

$L(M = 1, N)$	Input Position ($x = W/2 - iW/N$)	Split Ratio
$N = 6$	$i = 1, 5$	62:33:5
$N = 6$	$i = 3$	33:33:33
$N = 7$	$i = 1, \dots, 6$	54:35:11
$N = 8$	$i = 2, 6$	50:25:25

The input position analysis followed the approach of Bachmann et al. [47]. Table 1 summarizes Bachmann’s results, highlighting unconventional three-way splitting ratios suitable for a tri-coupler implementation. Tapered access ports of $120\text{ }\mu\text{m}$ length and $5.85\text{ }\mu\text{m}$ width were positioned at $\pm 8.24\text{ }\mu\text{m}$ ($x = 2W/7.28$: between $N = 7$ and 8 from Tab. 1), balancing compactness and coupling efficiency with fabrication requirements (a gap between waveguides of $2\text{ }\mu\text{m}$). This position was determined through iterative simulations of the outer waveguide positions, whilst monitoring the three outer outputs for maximal light in the center output.

These three tri-coupler designs — the standard, tapered, and MMI — with the parameters above were compared for their suitability as exoplanet beam combiners and starlight attenuators.

3. Results

In this section, we compare the simulated performance of the three tri-coupler configurations, examining their null depth, exoplanet throughput, and potential sensitivity to fabrication errors. The expected propagation and radiative losses are also analyzed, and their influence on null performance.

The potential of each design for fringe tracking is investigated to assess how effectively the null can be maintained under varying phase conditions. All simulations are injected with TE fields, and the tri-couplers’ performance is measured in TE light. Finding optimal parameters for each tri-coupler that satisfy both polarizations is beyond the scope of this work. Future work will address TM performance since half of the light entering the chip from a telescope is expected to be TM. This will either use non-birefringent couplers or polarization splitters for a set of, separately, optimized couplers.

To understand how a tri-coupler can be used for nulling and fringe tracking, the light distributions at the output ports were simulated for a range of phase offsets between the two outer input waveguides, across the full operational bandwidth. The resulting normalized output intensities for the outer and central waveguides are shown in Fig. 3, normalized for lossless propagation.

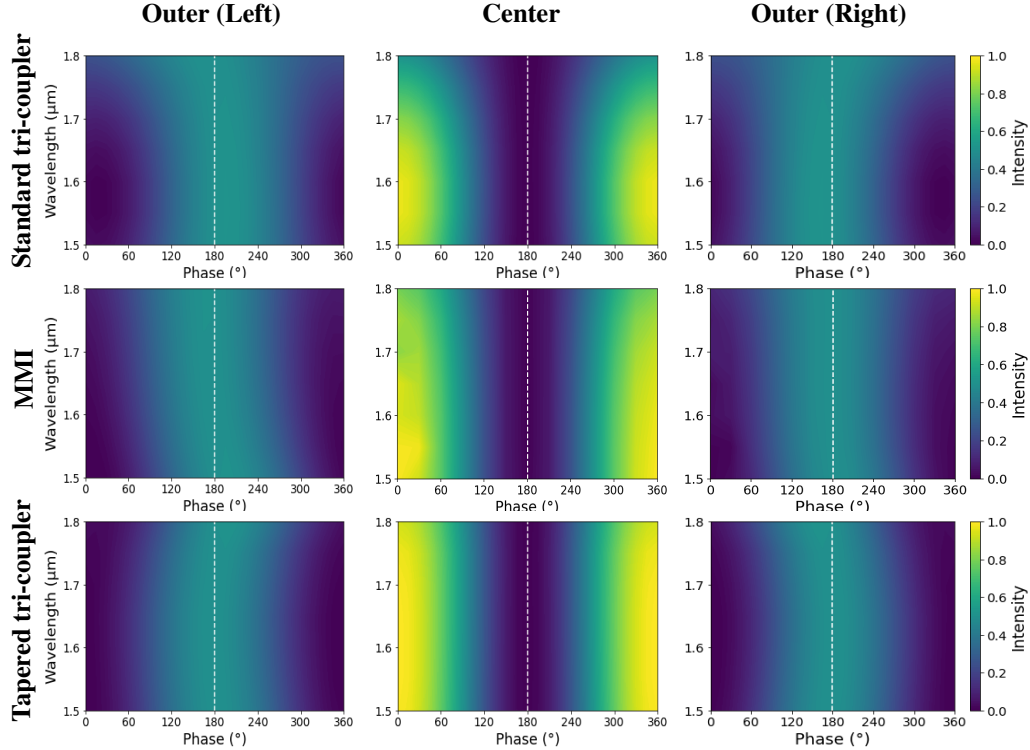


Fig. 3. Normalized intensity in the three tri-coupler configurations (Standard, MMI, and Tapered) for the left, center, and right output waveguides. Equal-intensity launch fields are injected into the two outer input ports across the full wavelength range as a function of phase difference.

Figure 3 presents the simulated intensity response of the three tri-couplers as a function of phase difference and wavelength. Each simulation injected two equal-intensity TE fields into the outer ports, and the power at each output waveguide was monitored using a square $10 \times 10 \mu\text{m}$ partial power monitor and normalized to the sum across all monitors. These monitors were selected to encompass the mode guided by the waveguide plus scattered light in the vicinity that may disturb the signal, which is especially important when discussing the null depth as will be shown later in Sec. 3.4.

All three devices exhibit similar phase-dependent responses. In each case, the central output port shows maximum transmission at a 0° phase offset and a deep null at 180° , consistent with the expected reciprocal symmetry. This null corresponds to destructive interference of the starlight, while the 0° peak represents exoplanet throughput. Beyond 180° , the response returns in a symmetric periodic pattern, demonstrating the full interferometric modulation across 360° .

For the left and right output ports, the responses are mirror images of one another. It is crucial for differential sensing that these responses do not overlap. As discussed in Sec. 3.3, a left and right peak offset from 180° will enable upstream modulation to deepen the starlight suppression. Only the tapered tri-couplers can strike a balance with the other metrics whilst maintaining

sensing across the bandwidth.

Focusing on the central port transmission, for exoplanet throughput, a wavelength-dependent roll-off is observed for both the standard tri-coupler and the MMI, indicating chromatic coupling behavior. In contrast, the tapered tri-coupler maintains an approximately constant response across the wavelength, consistent with its partially achromatic design. This is better examined using a cross-section of the exoplanet throughput.

3.1. Exoplanet Throughput

The maximum light transmission into the central output occurs when two equal-intensity electric fields are launched into the outer waveguides with a 0° phase difference. As shown in the central panels of Fig. 3, each tri-coupler exhibits a distinct degree of chromaticity in its exoplanet throughput under this condition.

Figure 4 presents wavelength cross-sections at 0° phase offset: the light in the central output port, normalized to the light in all three output ports. The standard tri-coupler reaches peak intensity near $1.55 \mu\text{m}$, corresponding to its design wavelength. The MMI demonstrates weaker wavelength de

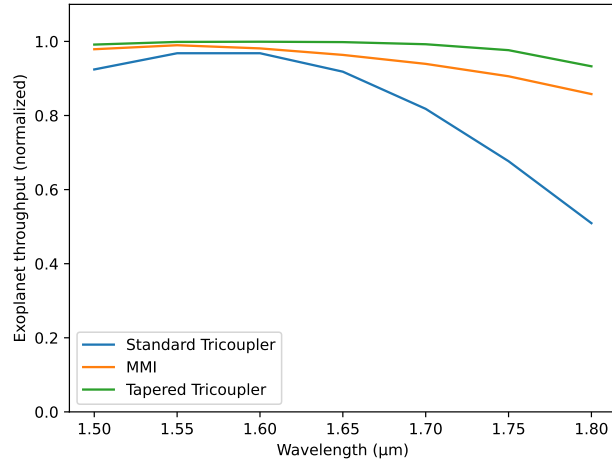


Fig. 4. Comparison of constructive interference in the central output when injecting equal-intensity electric fields with a 0° phase difference into the outer waveguides, for the three tri-coupler designs, normalized to total transmission.

These results show that both the MMI and tapered tri-couplers achieve higher exoplanet throughput than the standard design, with the tapered configuration offering the best overall performance. Despite a minor drop in intensity at longer wavelengths, the tapered tri-coupler maintains nearly 100% transmission across the full bandwidth. The MMI remains above 85%, while the standard tri-coupler performance declines to approximately 50% at higher wavelengths.

Note that these results exclude propagation and radiative losses, which will further influence the actual exoplanet throughput.

3.2. Component and bend losses

A major distinction between the evanescent tri-couplers and the MMI design is the loss. The evanescent couplers are effectively lossless ($<0.01 \text{ dB} \approx 0.3\%$ loss), except for the radiative losses introduced by the bent waveguides that connect the coupling region to the rest of the chip, the subject of this section.

In contrast, MMIs are known to exhibit higher and more wavelength-dependent losses, particularly when optimized for equal splitting across a broad bandwidth [48, 49]. This

wavelength dependence arises from the beat-length relationship described in Eq. (5), which predicts maximum transmission near the design wavelength (1.55 μm) and reduced transmission at shorter and longer wavelengths.

Figure 5 compares the simulated total losses of all three tri-couplers, including the bends into and out of each device, and assuming no losses from the material. The MMI displays a narrow region of low loss comparable to the other designs (shifted in wavelength by the custom outer waveguide pos

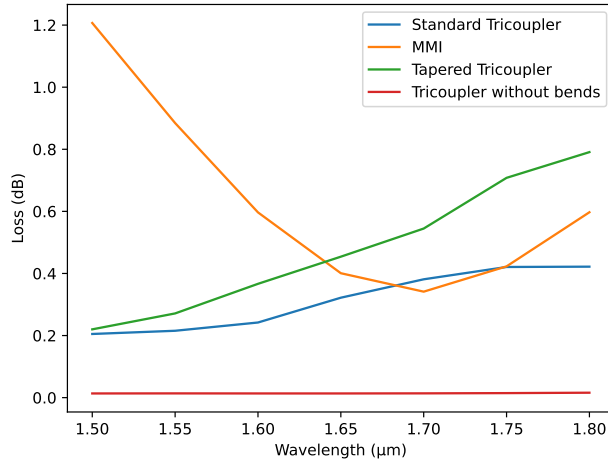


Fig. 5. Simulated loss of the MMI (orange) compared with the standard tri-coupler (green), tapered tri-coupler (blue), and a standard tri-coupler without bends (red).

The “no-bend” tri-coupler represents an idealized (impossible in reality) case in which the waveguides begin and end at 2 μm and remain without deviation throughout the simulation. This configuration exhibits negligible loss of 0.014 dB (0.3%), due to near-perfect overlap between the waveguide fundamental modes and the supermodes of the coupling region. When bends are introduced, both evanescent designs exhibit increasing loss with wavelength. This trend reflects bend-induced radiation, as larger wavelengths correspond to larger mode sizes and consequently greater leakage in curved sections.

The tapered tri-coupler has slightly higher loss than the standard design, primarily because one set of bent waveguides narrows to smaller widths, which have greater loss than the standard waveguide bends, and another set with larger widths, which may excite higher-order modes that radiate from the bend. The standard waveguide junction loss for an 850 μm bend radius was calculated in RSoft FemSIM at 0.16 dB (3.6%) at 1.55 μm but 0.62 dB (13.4%) at 1.8 μm , the latter higher than what was recorded in the standard tri-coupler and MMI. This reflects the difference between losses from a finite element simulation and from the beam propagation method. It does, however, indicate that the two evanescent tri-couplers are likely due to the bend losses. The MMI, by contrast, exhibits substantially higher intrinsic loss, starting at approximately 1.2 dB (24%) and decreasing to 0.3 dB (7%) at its optimized wavelength.

3.3. Use case for fringe tracking

The rejected starlight exiting the outer ports of the tri-coupler can be used to sense phase errors and drive a control loop to stabilize the null, effectively functioning as an on-chip fringe tracker. This sensing mechanism leverages the differential response of the outer outputs: as the phase deviates from the nominal 180° offset, the intensities in the two ports vary in opposite directions — one increases while the other decreases. The sign of this differential change indicates the direction of the phase error, while its magnitude reflects the error amplitude.

Maximum sensitivity is achieved when the intensity response curves of the two outer ports are offset such that their steepest gradients occur near 180° . Conversely, when the two curves overlap and both reach a peak or trough at 180° , the system enters a degenerate state in which no phase discrimination is possible.

Figure 6 illustrates two examples of the MMI's sensing behavior at wavelengths of $1.5 \mu\text{m}$ and $1.6 \mu\text{m}$. At $1.5 \mu\text{m}$ (Fig. 6a), the outer-port intensities exhibit a clear differential response, allowing effective fringe tracking. In contrast, at $1.6 \mu\text{m}$ (Fig. 6b), the responses are degenerate, making the coupler unsuitable for sensing at that wavelength.

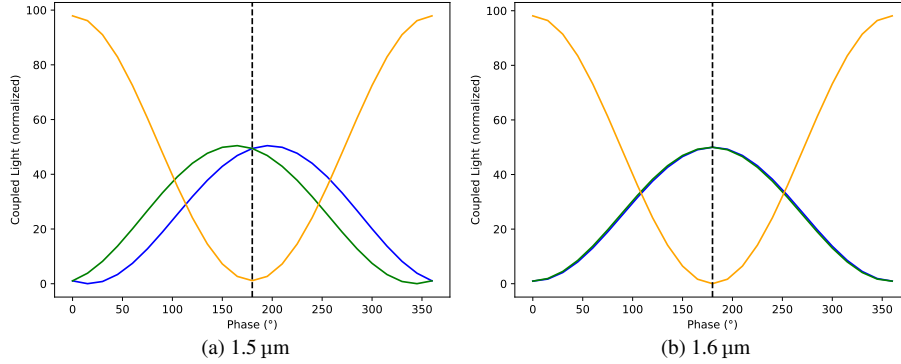


Fig. 6. Cross-sections from Fig. 3 showing the MMI transmission maps at (a) $1.5 \mu\text{m}$ and (b) $1.6 \mu\text{m}$.

This behavior is similar to tri-couplers written in ULI that either have degeneracy at 1.4 or $1.55 \mu\text{m}$ when optimized [50]. Multiple non-degenerate wavelengths enable phase-wrap tracking. The more spectral channels, the better the wavefront sensing. It's not strictly necessary for all wavelengths used in wavefront sensing, but doing so, and having a slope distinct from $0\%/^\circ$, will improve overall performance by increasing the signal-to-noise ratio. The objective is to find a tri-coupler without degeneracy over the bandwidth.

The slope, the derivative, of either outer port's intensity response at 180° provides a simple metric for identifying degeneracy. Figure 7 shows the slope of the left outer port for each tri-coupler design. The standard tri-coupler and MMI both exhibit large initial slopes, indicating strong sensitivity, before passing through zero slope, where the outputs become degenerate at that wavelength, and then transitioning to negative slope, corresponding to a reversal of the left and right port responses relative to Fig. 6a. The tapered tri-coupler behaves differently, crossing the degeneracy line twice and remaining close to $0\%/^\circ$ until the $1.75 \mu\text{m}$ wavelength.

A second tapered tri-coupler, like that in Fig. 1b with a $400 \mu\text{m}$ length, a central waveguide of $3 \mu\text{m}$ and tapered outer waveguide from 2 to $5 \mu\text{m}$ was included in Fig. 7 to demonstrate a configuration that avoids degeneracy entirely. Although this design was not optimized for exoplanet throughput, it enables continuous fringe tracking across the entire bandwidth, thereby improving overall system sensitivity.

Changing the parameters of the other tri-couplers may shift the degeneracy point outside this waveband [50], but due to these couplers' dependence on L_π , from Eq. (4) and (5), they will not be able to have a slope response like tapered tri-coupler 2.

If changing the tapered tri-coupler's outer arm widths and increasing the coupling length is sufficient to avoid degeneracy, at the cost of exoplanet throughput, future work could further optimize the tapered coupler by exploring its full parameter space, potentially regaining much of the lost throughput, but this lies beyond the scope of the present study.

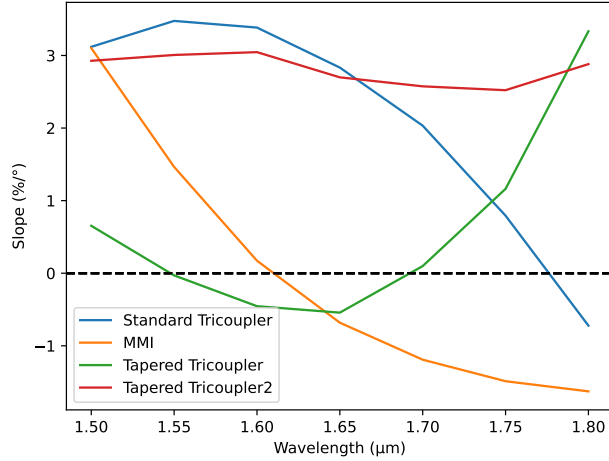


Fig. 7. Comparison of the outer-left-port slope at 180° phase offset for the three tri-couplers, including an additional tapered design.

3.4. Starlight attenuation performance and fabrication tolerance

In the case where the exoplanet's position is unknown, it may appear at any phase difference, corresponding to either a bright or dark fringe of the interferometric signal (the central output in Fig. 3), for example. Other injection configurations may inject incoherent exoplanet light or coherent exoplanet light at unequal intensities. Hence, a focus on attenuating the starlight is also required, increasing the exoplanet to starlight's SNR.

The measurable starlight attenuation is limited both intrinsically, by radiative light from bends and the scattered light from the components, specifically the MMI, and extrinsically, by fabrication imperfections such as waveguide asymmetry and under-etching. The following simulations quantify both effects.

The scattered light from a starlight injection was simulated as a point-source input equally into the two outer input ports with a 180° phase offset. Ideally, the null depth in the tri-coupler simulations, constructed mathematically, should be limited only by the simulation's numerical precision floor of approximately 80 dB (10^{-8} : the smallest number detected at the simulations' beginning). However, the destructive interference in the simulations' central output waveguide was limited by scattered light.

Figure 8 presents four scattered light simulations at a $1.55 \mu\text{m}$ wavelength: two standard tri-couplers and two MMIs, with bend radii of 0.4 mm and 92 mm.

In all cases, except for the standard tri-coupler with a large bend radius (Fig. 8d), scattered light is evident around the central extinction (at $X\text{-Position} = 0 \mu\text{m}$), reducing the achievable starlight attenuation, as defined by Eq. (1), to approximately 30 dB (10^{-3}).

The standard tri-coupler simulations (Figs. 8c and 8d) demonstrate the effect of bend radii on radiative light, showing a two-order-of-magnitude reduction in scattered light when the bend radius increases from 0.4 mm to 92 mm — although there is evidence of scattered light remaining around the center line for the larger bend radius coupler, as shown at $Z\text{-Positions}$ 3000 to 5000 μm , which will reduce the measurable null depth.

For the MMI, radiative scattering from light not coupled into the outer tapers is the dominant factor limiting attenuation. Comparing Figs 8b and 8d, the scattered light intensity also differs by roughly two orders of magnitude. While further optimization could increase confinement in the MMI, wavelength dependence ensures scattered light will reappear across the band.

To mitigate this effect, the output ports could be physically rerouted, displacing their output

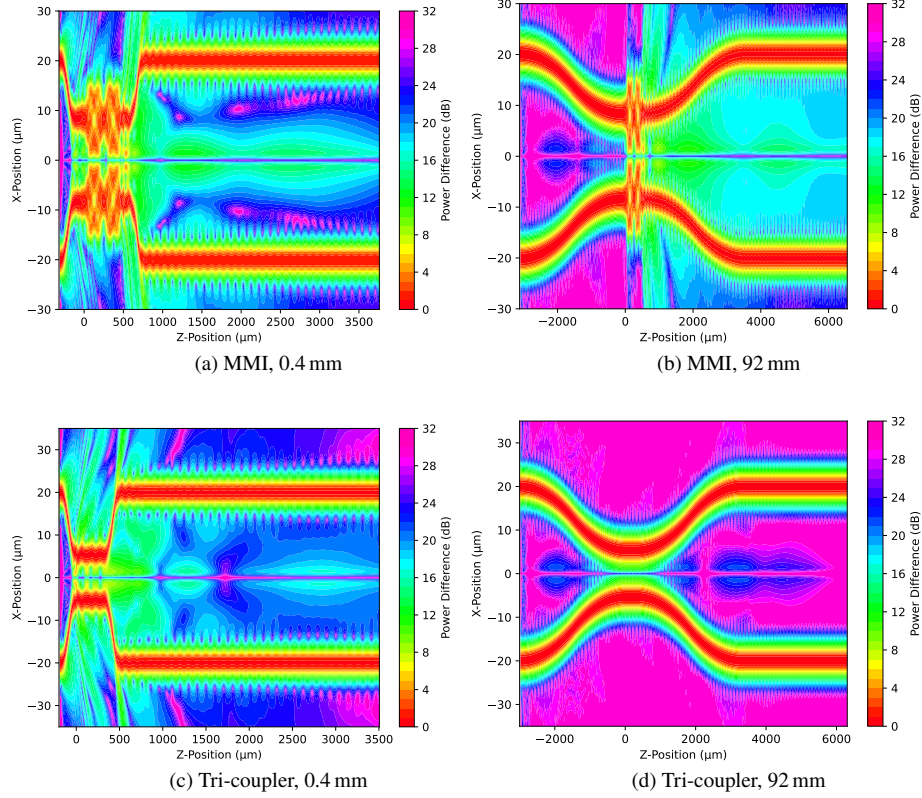


Fig. 8. Simulated scattered light (normalized) for MMIs with (a) 0.4 mm and (b) 92 mm bend radii, and standard tri-couplers with (c) 0.4 mm and (d) 92 mm bend radii.

facets away from scattered-light regions. This approach would require careful chip layout to avoid overlap between scattered fields and the output ports.

While scattered light imposes a fundamental limitation on the achievable attenuation, fabrication imperfections introduce additional degradation, often exceeding the simulated scattering effects. The following analysis quantifies the impact of these fabrication errors on the tri-couplers' starlight attenuation performance and exoplanet throughput.

Consider what an asymmetry, due to an imperfection in the fabrication or in the waveguide position, will do to the attenuation. Figure 9 compares the attenuation of all three tri-couplers when the right-most waveguide is laterally shifted by $\pm 0.1 \mu\text{m}$. For the MMI, this shift corresponds to the input position within its broad central region, with the reciprocal output position shifted accordingly.

For the tolerance analysis simulations, long bent waveguides were added to the tri-coupler output, in otherwise 10 dB (10^{-1}) scattered light-limited simulations (just as Fig. 8c, to allow scattered light to disperse and to shake any uncoupled light overlapping the central output port. For the ideal (defect-free) designs, the attenuation remained limited by scattered light, beginning at 40 dB (10^{-4}) (the MMI) near $1.5 \mu\text{m}$ and improving to between 50 dB (10^{-5}) (the standard tri-coupler) and 60 dB (10^{-6}) (the tapered tri-coupler) at longer wavelengths. Potentially, a longer bend would further decrease these values, but for starlight attenuation limitations, these bends are sufficient.

Figure 9 shows that the MMI is the least affected by positional asymmetry, remaining below 40 dB. The standard and tapered tri-coupler degrades to between 20 dB (10^{-2}) and 30 dB (10^{-3}).

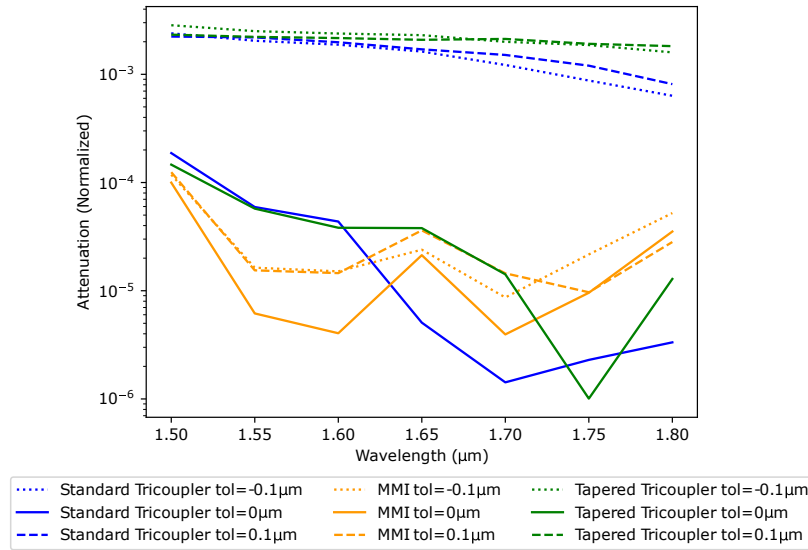


Fig. 9. Simulated attenuation for each tri-coupler with a $\pm 0.1 \mu\text{m}$ lateral shift of the right-most waveguide.

Comparatively, the null depth achieved in the tri-couplers used in GLINT was between 30 and 40 dB [51], placing this work in a good position if asymmetric fabrication can be avoided.

A more common fabrication issue is a uniform reduction in waveguide width due to under-etching [52]. This type of error preserves the overall symmetry and therefore the star extinction, but it affects the exoplanet light. Figure 10 shows the percentage change in exoplanet throughput when all waveguide widths are uniformly reduced by $0.1 \mu\text{m}$.

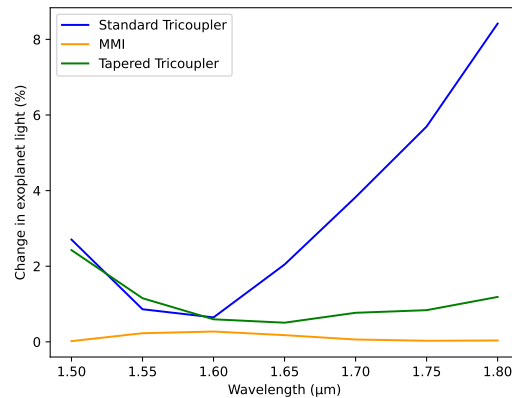


Fig. 10. Change in exoplanet light for each tri-coupler when all waveguide widths are reduced by $0.1 \mu\text{m}$.

The tapered tri-coupler exhibits an average 1% change in exoplanet light, reaching $>2\%$ at the spectral extremes. The standard tri-coupler shows a stronger wavelength dependence, beginning with a 2% change at short wavelengths and increasing up to an apparent 8% gain at longer wavelengths. This, for the standard tri-coupler, corresponds to a shift of the constructive

interference peak in wavelength — caused by changes in the beat length resulting from the modified waveguide width and separation.

In contrast, the MMI shows negligible change, consistent with the large multimode region’s inherent tolerance. This confirms the MMI’s robustness to common fabrication errors, albeit at the cost of a higher intrinsic loss than the evanescent tri-couplers.

Overall, the achievable attenuation in on-chip tri-couplers is limited by scattered light, bend-induced radiation, and fabrication imperfections. Among the designs studied, the tapered tri-coupler offers the best balance between attenuation and achromaticity while maintaining on-chip fringe tracking, albeit with reduced fabrication tolerance.

4. Discussion

The results discussed in Sec. 3, and summarized in Tab. 2, focused on the exoplanet light, the starlight attenuation, and sensing, all three of which are important for exoplanet detection.

Table 2. Summary of significant results, where η_p and η_s are normalized to the total transmission.

Metric (at $1.55 \mu\text{m}$ $\begin{matrix} + \text{ highest value} \\ - \text{ lowest value} \end{matrix}$)	Standard	MMI	Tapered
Exoplanet transmission at $\lambda/2D$ (η_p :%)	97 $^{+0}_{-47}$	99 $^{+0}_{-14}$	100 $^{+0}_{-6}$
Starlight attenuation (η_s :dB)	42 $^{+17}_{-5}$	52 $^{+2}_{-12}$	53 $^{+7}_{-15}$
Below 40 dB (nm)	270	300	280
Attenuation depth fabrication deviation (dB)	27 $^{+4}_{-1}$	48 $^{+3}_{-9}$	27 $^{+1}_{-1}$
Below 40 dB (nm)	0	290	0
Loss (dB)	0.2 $^{+0.4}_{-0}$	0.9 $^{+0.3}_{-0.6}$	0.25 $^{+0.55}_{-0.05}$
Fringe tracking non-degeneracy	no	no	yes*
Scattered light mitigation	yes	no	yes

*Can be obtained with different parameters.

From the standard tri-coupler to the MMI to the tapered tri-coupler, we have seen an increase in achromaticity for exoplanet light throughput, and the starlight attenuation is already achromatic. The MMI and tapered tri-coupler transmit nearly 100% of the exoplanet light at all wavelengths. Achromaticity was also found in sensing, but only for a second tapered tri-coupler that was not optimized for exoplanet throughput.

For each coupler in this paper, sensing is possible, but not for every wavelength. For the tapered tri-coupler, the sensing is near degenerate ($0^\circ/^\circ$ slope) most of the waveband, making sensing difficult. This may be because this coupler was optimized for high exoplanet throughput. A second tapered tri-coupler was included to prove the possibility of creating a tri-coupler without degeneracy.

For the standard tri-coupler, the sensing response and exoplanet light are linked: the area of best sensing corresponds with the highest exoplanet throughput. The other tri-couplers do not corroborate this. The MMI’s link between the exoplanet light and sensing is not as clear-cut as the standard tri-coupler, and the tapered tri-coupler has the opposite relation between sensing and exoplanet throughput: moving away from a zero slope when the exoplanet light decreases from 100%. From these examples, we see no clear link between sensing and exoplanet throughput, leaving the possibility for an achromatic tapered tri-coupler in exoplanet throughput and a non-degenerate slope with the correct selection of variables.

The loss simulations compared the total MMI loss to the bend losses for the otherwise lossless evanescent tri-couplers. The MMI has the highest loss of the three tri-couplers, with up to 20% (0.9 dB) loss occurring at 1.55 μm but decreased to 7% (0.3 dB) at 1.7 μm . The evanescent couplers have bend losses into and out of the coupling region. This can be mitigated by increasing the bend radii of the input and output bends. The tapered waveguide has higher losses due to the smaller waveguides in the input bends and the larger waveguides in the output bends. Increasing the bend radius will reduce the light lost by the smaller waveguides. An increased bend radius has the downside of increasing coupling before the coupling length and can be accounted for in the standard tri-coupler by decreasing the coupling length. For the tapered tri-coupler, coupling occurring in the bends will change the response over the bandwidth and requires a large parameter scan to re-optimize.

Despite the high losses, the MMI is a viable choice due to its robust tolerance to common fabrication errors. Ideally, the starlight attenuation will only be affected by scattered light from radiative light from bends. This limits our attenuation, and why the tri-couplers' output ports are recommended to be redirected outside the scattered-light zone. For standard waveguides, the bend losses were simulated at 0.16 dB/junction at 1.55 μm , and an increase in bend radius would reduce these further, decreasing the scattered light in the other tri-couplers.

The attenuation was tested against a common issue of asymmetry — changing the gap between the center and right waveguides by 0.1 μm . The tolerance analysis shows that asymmetric gaps between waveguides reduce the attenuation for each tri-coupler to more than the scattered light intensity. The MMI is least affected by asymmetry but is still restricted to 40 dB (10^{-4}) by the fabrication error.

Without defect, the three tri-couplers have > 40 dB attenuation over a > 270 nm bandwidth. With defects, only the MMI achieves a starlight attenuation > 40 dB. This attenuation establishes parity between starlight and light from a young Jupiter-like exoplanet, improving detectability.

The exoplanet light is affected by fabrication limitations with shrinkage resulting in up to 8% less throughput for the standard tri-coupler. The other tri-couplers are much more robust to shrinkage, with only 2% more exoplanet light lost in the tapered tri-coupler and an insignificant amount for the MMI. This is a symmetric change and won't affect the null as drastically as the asymmetric error.

The MMI appeared as a reasonable alternative to the standard tri-coupler. When accounting for sensing, both the standard tri-coupler and MMI cross the slope and become degenerate. This will limit the sensing bandwidth, and only the tapered tri-coupler, not optimized for exoplanet throughput, has no degeneracy. Comparing only the MMI and the tapered tri-coupler, the MMI appears advantageous given common fabrication defect tolerances, but suffers from higher losses than the other tri-couplers.

What has not been explored in this paper are sub-wavelength gratings [53], previously used to create ultra-broadband couplers [54], and inverse design approaches [55]. These technologies could be leveraged to realize broadband couplers and may be used in future work to improve these tri-couplers (both evanescent and MMI). They employ nanophotonic structuring to maintain consistent optical behavior across the waveband. With the advent of neural-network-based optimization, it is now possible to generate either “black-box” devices [56] or modified variants of existing couplers [57] to produce custom nulling interferometers. While these approaches are beyond the scope of the present work, they are promising directions for future development.

5. Conclusion

High-contrast imaging enables the detection and characterization of exoplanets far fainter than their host stars. This is typically achieved in interferometry by using multiple telescopes or by using segments of a single telescope, so that stellar light is attenuated while the residual signal is measured. In coronagraphy, the star is blocked/attenuated, and exoplanet light is allowed through.

This work has demonstrated that three different tri-couplers can achieve achromatic starlight attenuation and exoplanet throughput in a two-dimensional photonic platform for use after either high-contrast imaging methods.

To increase exoplanet throughput, the standard evanescent tri-coupler should be replaced with either an MMI or a tapered evanescent tri-coupler. Both can be optimized to increase exoplanet throughput without compromising on the starlight attenuation.

A novel MMI design was proposed that combines the symmetric MMI mode with general MMI interference between $N = 7$ and 8, utilizing injection positions of $\pm 8.24 \mu\text{m}$. This reduces the MMI length to a scale comparable to the tri-coupler. However, it introduces additional losses compared to evanescent couplers, which are only limited by bend losses. These MMI losses, combined with radiative bending loss, limit exoplanet detection due to starlight scattered into the destructive interference output ports. This necessitates careful routing of the output waveguides to mitigate this noise in the exoplanet detection.

The tapered tri-coupler was optimized for exoplanet throughput across the $1.5\text{--}1.8 \mu\text{m}$ waveband. Unlike typical broadband tapered devices that rely on strict adiabaticity, this design, as a splitter, uses a compact design and exploits an extended coupling region into the outer arms.

In terms of sensing, none of the couplers provides perfectly achromatic performance. However, an example tapered coupler demonstrated an achromatic, high-sensing response across the full waveband, at the expense of some exoplanet throughput. This suggests that designs may exist that achieve both high throughput (though not necessarily 100%) and strong sensing capability.

Experimental validation is essential to confirm these predictions. Tri-couplers are highly sensitive to fabrication tolerances, with deviations in waveguide width or asymmetry leading to significant 20 to 30 dB stellar leakage into the central waveguide. The MMI design is more robust to such errors, maintaining 40 dB starlight attenuation over the bandwidth. This makes the MMI the preferred component for assessing the science case of a high contrast imaging instrument until tapered tri-couplers can be fabricated with high precision.

Future work will focus on experimental verification of these components, assessing fabrication performance, starlight attenuation, exoplanet throughput, and sensing — to evaluate their potential for fringe tracking. Further exploration of the tapered coupler parameter space may enhance performance across all three metrics. Establishing a link between the taper slope and sensing response, and optimizing the coupler length accordingly, could provide insight into the relationship between sensing and exoplanet throughput, and whether they can be improved simultaneously or are fundamentally constrained by a trade-off.

Beyond geometric optimization, incorporating sub-wavelength grating engineering or inverse-designed photonic structures offers a promising route toward achieving intrinsically broadband behavior, representing a natural next stage for this work.

6. Acknowledgments

This work was supported by the National Aeronautics and Space Administration (NASA) under grant number 80NSSC24K1559, awarded through the Astrophysics Research and Analysis (APRA) program. This work was supported by the National Science Foundation under Grant numbers 2308360 and 2308361.

7. Disclosures

The authors declare no conflicts of interest.

References

1. A. Wolszczan and D. A. Frail, “A planetary system around the millisecond pulsar PSR1257 + 12,” *Nature* **355**, 145–147 (1992).

2. B. Lyot, "A study of the solar corona and prominences without eclipses," *Mon. Notices Royal Astron. Soc.* **99**, 580 (1939).
3. R. N. Bracewell, "Detecting nonsolar planets by spinning infrared interferometer," *Nature* **274**, 780–781 (1978).
4. C. Marois, D. Lafreniere, R. Doyon, *et al.*, "Angular differential imaging: A powerful high-contrast imaging technique," *The Astrophys. J.* **641**, 556–564 (2006).
5. D. Echeverri, J. W. Xuan, J. D. Monnier, *et al.*, "Vortex fiber nulling for exoplanet observations: First direct detection of m dwarf companions around HIP 21543, HIP 94666, and HIP 50319," *The Astrophys. J. Lett.* **965**, L15 (2024).
6. R. Errmann, S. Minardi, L. Labadie, *et al.*, "Integrated optics interferometric four telescopes nuller," *Appl. Opt.* **54**, 7449–7454 (2015).
7. Y. Xin, N. Jovanovic, G. Ruane, *et al.*, "Efficient detection and characterization of exoplanets within the diffraction limit: Nulling with a mode-selective photonic lantern," *The Astrophys. J.* **938**, 140 (2022).
8. J. Bland-Hawthorn and P. Kern, "Astrophotonics: a new era for astronomical instruments," *Opt. Express* **17**, 1880 (2009).
9. J. J. Bryant, R. R. Thomson, and M. J. Withford, "Focus issue introduction: recent advances in astrophotonics," *Opt. Express* **25**, 19966 (2017).
10. A. N. Dinkelaker, A. Rahman, J. Bland-Hawthorn, *et al.*, "Astrophotonics: introduction to the feature issue," *J. Opt. Soc. Am. B* **38**, AP1 (2021).
11. N. Jovanovic, P. Gatkine, N. Anugu, *et al.*, "2023 astrophotonics roadmap: pathways to realizing multi-functional integrated astrophotonic instruments," *J. Phys. Photonics* **5**, 042501 (2023).
12. S. Gillesen, F. Eisenhauer, G. Perrin, *et al.*, "GRAVITY: a four telescope beam combiner instrument for the VLTI," in *Optical and Infrared Interferometry II*, vol. 7734 (SPIE, 2010), p. 77340Y.
13. G. Perrin, S. Lacour, J. Woillez, and E. Thiebaut, "High dynamic range imaging by pupil single-mode filtering and remapping," *Mon. Notices Royal Astron. Soc.* **373**, 747–751 (2006).
14. K. Barjot, E. Huby, S. Vievard, *et al.*, "Laboratory characterization of FIRSTv2 photonic chip for the study of substellar companions," in *Optical and Infrared Interferometry and Imaging VII*, vol. 11446 (SPIE, 2020), p. 1144623.
15. E. Huby, G. Perrin, F. Marchis, *et al.*, "FIRST, a fibered aperture masking instrument: i. first on-sky test results," *Astron. Astrophys.* **541**, A107 (2012).
16. E. Huby, G. Duchêne, F. Marchis, *et al.*, "FIRST, a fibered aperture masking instrument: ii. spectroscopy of the capella binary system at the diffraction limit," *Astron. Astrophys.* **560**, A113 (2013).
17. B. Norris, N. Cvetojevic, S. Gross, *et al.*, "High-performance 3d waveguide architecture for astronomical pupil-remapping interferometry," *Opt. Express* **22**, 18335–53 (2014).
18. E. Arcadi, G. Douglass, J. Webb, *et al.*, "Design, fabrication and characterisation of a 3-baseline, achromatic integrated optics beam combiner for nulling interferometry with simultaneous fringe tracking using tricouplers," in *Advances in Optical and Mechanical Technologies for Telescopes and Instrumentation VI*, vol. 13100 (SPIE, 2024), p. 94.
19. G. Garreau, A. Bigioli, R. Laugier, *et al.*, "Asgard/NOTT: L-band nulling interferometry at the vlti. ii. warm optical design and injection system," *J. Astron. Telesc. Instruments, Syst.* **10**, A110 (2024).
20. A. Sanny, L. Labadie, S. Gross, *et al.*, "Asgard/nott: L-band nulling interferometry at the vlti," *Astron. & Astrophys.* **705**, A37 (2026).
21. T. Gretzinger, S. Gross, A. Arriola, and M. J. Withford, "Towards a photonic mid-infrared nulling interferometer in chalcogenide glass," *Opt. Express* **27**, 8626 (2019).
22. M.-A. Martinod, P. Tuthill, S. Gross, *et al.*, "Achromatic photonic tricouplers for application in nulling interferometry," *Appl. Opt.* **60**, D100 (2021).
23. G. Douglass, E. Arcadi, S. Rossini-Bryson, *et al.*, "Passive achromatic phase shifter fabricated using ultrafast laser inscription," *J. Light. Technol.* **43**, 4416–4421 (2025).
24. T. Gretzinger, S. Gross, M. Ams, *et al.*, "Ultrafast laser inscription in chalcogenide glass: thermal versus athermal fabrication," *Opt. Mater. Express* **5**, 2862–2877 (2015).
25. R. A. Bernstein, P. J. McCarthy, K. Raybould, *et al.*, "Overview and status of the Giant Magellan Telescope project," in *Ground-based and Airborne Telescopes V*, vol. 9145 (SPIE, 2014), p. 91451C.
26. C. Dressing, M. Ansdell, J. Croke, *et al.*, "The Habitable Worlds Observatory: Status, Plans, and Opportunities," *Bull. AAS* **56** (2024).
27. H.-D. Kenchington Goldsmith, N. Cvetojevic, M. Ireland, *et al.*, "Chalcogenide glass planar MIR couplers for future chip based bracewell interferometers," in *Optical and Infrared Interferometry and Imaging V*, vol. 9907 (SPIE, 2016), p. 990730.
28. H.-D. Kenchington Goldsmith, M. Ireland, P. Ma, *et al.*, "Photonic mid-infrared nulling for exoplanet detection on a planar chalcogenide platform," in *Optical and Infrared Interferometry and Imaging VI*, vol. 10701 (SPIE, 2018), p. 33.
29. C. V. Morley, H. Knutson, M. Line, *et al.*, "Forward and inverse modeling of the emission and transmission spectrum of gj 436b: Investigating metal enrichment, tidal heating, and clouds," *The Astron. J.* **153**, 86 (2017).
30. P. A. Besse, M. Bachmann, and H. Melchior, "New 1x2 MMI with free selection of power splitting ratios," in *20th European Conference on Optical Communication*, (1994), pp. 669–672.
31. P. Gatkine, G. Sercel, N. Jovanovic, *et al.*, "Efficient ultra-broadband low-resolution astrophotonic spectrographs," *Opt. Express* **32**, 17689–17703 (2024).

32. H. kai Hsiao, K. A. Winick, J. D. Monnier, and J.-P. Berger, "An infrared integrated optic astronomical beam combiner for stellar interferometry at 3-4 microns," *Opt. Express* **17**, 18489 (2009).
33. Synopsys, Inc, "Rsoft photonic device tools," .
34. G. Ruane, J. Wang, D. Mawet, *et al.*, "Efficient spectroscopy of exoplanets at small angular separations with vortex fiber nulling," *The Astrophys. J.* **867**, 143 (2018).
35. E. Serabyn, J. K. Wallace, G. J. Hardy, *et al.*, "Deep nulling of visible laser light," *Appl. Opt.* **38**, 7128–7132 (1999).
36. C. Hanot, B. Mennesson, S. Martin, *et al.*, "Improving interferometric null depth measurements using statistical distributions: Theory and first results with the palomar fiber nuller," *The Astrophys. J.* **729**, 110 (2011).
37. I. Snellen, R. de Kok, J. L. Birkby, *et al.*, "Combining high-dispersion spectroscopy with high contrast imaging: Probing rocky planets around our nearest neighbors," *Astron. & Astrophys.* **576**, A59 (2015).
38. K. L. Kruse and C. T. Middlebrook, "Fan-out routing and optical splitting techniques for compact optical interconnects using single-mode polymer waveguides," *J. Mod. Opt.* **62**, S1–S10 (2015).
39. J. Donnelly, "Limitations on power-transfer efficiency in three-guide optical couplers," *IEEE J. Quantum Electron.* **22**, 610–616 (1986).
40. H. kai Hsiao, K. A. Winick, and J. D. Monnier, "Midinfrared broadband achromatic astronomical beam combiner for nulling interferometry," *Appl. Opt.* **49**, 6675 (2010).
41. A. F. Milton and W. K. Burns, "Tapered velocity couplers for integrated optics: Design," *Appl. Opt.* **14**, 1207 (1975).
42. R. B. Smith, "Analytic solutions for linearly tapered directional couplers," *J. Opt. Soc. Am.* **66**, 882–892 (1976).
43. A. Takagi, K. Jinguji, and M. Kawachi, "Wavelength characteristics of (2 x 2) optical channel-type directional couplers with symmetric or nonsymmetric coupling structures," *J. Light. Technol.* **10**, 735–746 (1992).
44. T. A. Ramadan, R. Scarmozzino, and R. M. Osgood, "Adiabatic couplers: Design rules and optimization," (1998).
45. O. Bryngdahl, "Image formation using self-imaging techniques," *J. Opt. Soc. Am.* **63**, 416–419 (1973).
46. L. B. Soldano and E. C. M. Pennings, "Optical multi-mode interference devices based on self-imaging: principles and applications," *J. Light. Technol.* **13**, 615–627 (1995).
47. M. Bachmann, P. A. Besse, and H. Melchior, "Overlapping-image multimode interference couplers with a reduced number of self-images for uniform and nonuniform power splitting," *Appl. Opt.* **34**, 6898–910 (1995).
48. H.-D. Kenchington Goldsmith, N. Cvetojevic, M. Ireland, and S. Madden, "Fabrication tolerant chalcogenide mid-infrared multimode interference coupler design with applications for bracewell nulling interferometry," *Opt. Express* **25**, 3038 (2017).
49. H.-D. Kenchington Goldsmith, M. Ireland, P. Ma, *et al.*, "Improving the extinction bandwidth of mmi chalcogenide photonic chip based mir nulling interferometers," *Opt. Express* **25**, 16813–16824 (2017).
50. T. Kliner-Teo, M.-A. Martinod, P. Tuthill, *et al.*, "Achromatic design of a photonic tricoupler and phase shifter for broadband nulling interferometry," *J. Astron. Telesc. Instruments, Syst.* **8**, 045001 (2022).
51. M. A. Martinod, B. Norris, P. Tuthill, *et al.*, "Scalable photonic-based nulling interferometry with the dispersed multi-baseline glint instrument," *Nat. Commun.* **12**, 2465 (2021).
52. P. Morrissey, H. Yang, R. Sheehan, *et al.*, "Design and fabrication tolerance analysis of multimode interference couplers," *Opt. Commun.* **340**, 26–32 (2015).
53. P. Cheben, R. Halir, J. H. Schmid, *et al.*, "Subwavelength integrated photonics," *Nature* **560**, 565–572 (2018).
54. A. Maese-Novo, R. Halir, S. Romero-García, *et al.*, "Wavelength independent multimode interference coupler," *Opt. Express* **21**, 7033 (2013).
55. K. Kojima, M. H. Tahersima, T. Koike-Akino, *et al.*, "Deep neural networks for inverse design of nanophotonic devices," *J. Light. Technol.* **39**, 1010–1019 (2021).
56. A. Y. Piggott, J. Lu, K. G. Lagoudakis, *et al.*, "Inverse design and demonstration of a compact and broadband on-chip wavelength demultiplexer," *Nat. Photonics* **9**, 374–377 (2015).
57. H. Chen, G. Su, X. Fu, and L. Yang, "Ultra-broadband and compact 2 x 2 3-dB silicon adiabatic coupler based on supermode-injected adjoint shape optimization," *Photonics* **10**, 1311 (2023).